Materials LAB

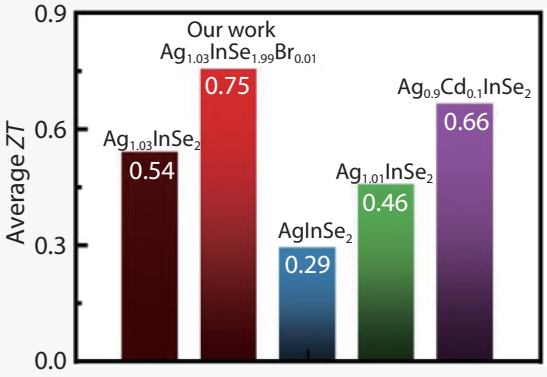
RESEARCH ARTICLE

Materials Lab 2024, 3, 230024

High performance of n-type thermoelectric material $AgInSe_2$ originated from strong acoustic phonon scattering

Shan Huang[1,†], Yan Wang[1,†], Baohai Jia[1], Yong Yu[1,2], Peijian Lin[1], Lin Xie[1*] and Jiaqing He[1*]

The chalcopyrite system, which consists of ABC_2 (where A can be Cu or Ag, B can be Ga or In, and C can be Se or Te), has potential uses in thermoelectric applications. However, the lack of high-performance n-type chalcopyrite thermoelectric has hindered their practical application. This study presents a new method for inhibiting cation vacancy in $AgInSe_2$, achieved through the addition of excessive amounts of Ag and Br doping, which further increases electronic concentration. The resulting n-type material, $Ag_{1.03}InSe_{1.99}Br_{0.01}$, exhibited superior thermoelectric performance at high temperatures, with a ZT of 1.2 at 900 K and an average ZT of 0.75 within a temperature range of 600-900 K. The remarkable thermal performance of this material is mainly due to its extremely low lattice thermal conductivity, which is attributed to the quartic anharmonicity and nondispersive phonon dispersion relation. These findings provide new insights into developing high-performance n-type chalcopyrite thermoelectric for practical use in energy conversion technologies.



Thermoelectric technology, which involves the conversion of heat into electrical power and vice versa, has gained significant attention as a potential solution to global energy issues. Thermoelectric devices, including refrigeration and power generation devices, have several attractive features, such as being noiseless, low-maintenance, emission-free, and reliable. The efficiency of thermoelectric devices is proportional to the figure of merit ($ZT = S^2\sigma T/\kappa$), where the S, σ, κ are the Seebeck coefficient, electrical conductivity, and thermal conductivity, respectively.[1] The total thermal conductivity κ can be described by the formula: $\kappa = \kappa_e + \kappa_{lat}$, where the κ_e and κ_{lat} is electronic thermal conductivity and lattice thermal conductivity, respectively. Additionally, the σ and κ_e obey the Wiedemann-Franz law, indicating a coupling relationship between electrical and thermal parameters [2].

To explore the decoupling of electronic and thermal transport in thermoelectrics, a number of strategies have been proposed to improve thermoelectric performance. These include defects manipulation, energy band convergence, strong spin-orbit coupling, strain, heterojunctions, nanostructures, and entropy engineering[3]. Among these methods, reducing lattice thermal conductivity is the most effective. For instance, low lattice thermal conductivity in room temperature (RT) thermoelectric Bi_2Te_3 can be achieved through the use of dense dislocation arrays[4]. Ultralow lattice thermal conductivity of medium-temperature thermoelectric chalcogenides can be induced by high entropy, and the lattice thermal conductivity of high-temperature thermoelectric SiGe alloys can be substantially reduced by employing nanostructures[5]. Recently, a group of chalcopyrite ABC_2 compounds (where A = Cu, Ag; B = Ga, In; and C = Se, Te) have drawn the attention of thermoelectric scientists due to their low lattice thermal conductivity. Examples of these compounds include $CuInSe_2$ (3.9 W m^{-1} K^{-1} at RT)[6], $CuGaTe_2$ (6.1 W m^{-1} K^{-1} at RT)[7], $CuInTe_2$ (5.8 W m^{-1} K^{-1} at RT)[8], $AgInSe_2$ (1.0 W m^{-1} K^{-1} at RT)[9], $AgGaTe_2$ (1.1 W m^{-1} K^{-1} at RT)[10], and $AgInTe_2$ (1.4 W m^{-1} K^{-1} at RT)[8]. Among the chalcopyrite compounds, Ag-based chalcopyrites exhibit lower lattice thermal conductivity, and $AgInSe_2$ has a much lower lattice thermal conductivity than other chalcopyrite compounds due to the weak chemical bonds in Ag-based chalcopyrites, which results in a lower sound velocity and enhanced Umklapp process[8,10].

The attainment of desirable thermoelectric properties

[1] *Department of Physics, Southern University of Science and Technology, Shenzhen 518055, China*

[2] *Department of Materials Science and Engineering, National University of Singapore 117575, Singapore*

* Corresponding author, E-mail: xiel3@sustech.edu.cn; hejq@sustech.edu.cn

Received 24 May 2023; Accepted 29 June 2023; Published online

†These authors contributed equally to this work

© 2024 The Author(s). *Materials Lab* published by Lab Academic Press

DOI: 10.54227/mlab.20230024

heavily relies on maintaining a low lattice thermal conductivity. The $AgInSe_2$ chalcopyrite has emerged as a prominent research material for its low lattice thermal conductivity[9,11,12]. Three-phonon (3ph) scattering, including the normal-mode process and Umklapp process, is generally considered to play a dominant role in thermal transport[13], however, the theory only includes 3ph scattering usually overestimate the lattice thermal conductivity of many traditional thermoelectric materials (including $AgInSe_2$)[14-17]. Despite the number of ongoing research, the fundamental explanation behind the low thermal conductivity is yet to be fully understood. Our previous research has shown that $AgCrSe_2$, another Ag-based material characterized by low lattice thermal conductivity with weakly Ag-bonded rattling constituents, exhibits strong four-phonon (4ph) scattering[12]. It inspires us to consider whether $AgInSe_2$, a material with similar composition and low thermal conductivity, may also exhibit strong 4ph scattering. In this study, our anharmonic lattice dynamics calculations and analysis of $AgInSe_2$ reveal that the strong localized phonon coupling is indeed due to 4ph interactions of low-frequency phonons in thermal transport. Including 4ph interaction, the lattice thermal conductivity of $AgInSe_2$ has been successfully predicted. We have found the impact of low-frequency optical phonons on thermal transport and resolve the issue of serious overestimation caused by 3ph interaction on lattice thermal conductivity in this work (which even led to the theoretical prediction value being more than twice the experimental value)[18-21].

Materials and methods

Synthesis

The $AgInSe_2$ samples were synthesized by mixing elements (High-purity Ag (99.999%), In (99.999%), Se (99.999%), and Br (99.999 %)) in stoichiometric proportions and reacting in a molten state, then spark plasma sintering into bulk. The total mass of each sample was about 8 g. The specific process is as follows: The mixtures of elements were sealed in evacuated silica tubes and heated to 1323 K at 100 K h^{-1}, kept at this temperature for 12 h, and quenched in cold water to room temperature; The samples were then annealed at 673 K under vacuum for 12 h before cooling to room temperature. The annealed ingots were crushed, and ground into a fine powder, followed by spark plasma sintering at 773–823 K under a pressure of 50 MPa for 5 min to obtain densified samples.

Measurement details

X-ray Diffraction: The obtained samples were analyzed by powder X-ray diffraction on a Rigaku smart lab system at 45 kV and 200 mA with Cu Kα radiation (LKα1 = 1.540593 Å, LKα2 = 1.544414 Å) at a scan rate of 2° min^{-1} and a step size of 0.020°.

Electron Microscopy: STEM experiments were conducted on a Thermofischer Themis G2 60-300 electron microscope under 300 kV. The convergence angle is 30 and the collection angle is 60-200 mrad, respectively. EDS mapping was conducted using a Super-X EDX detector.

Electronic Transport Measurements: For all samples (~2 × 2 × 8 mm^3), the electrical resistivity and Seebeck coefficient were simultaneously measured using a ZEM-3 system (Ulvac-Riko, Japan) under a helium atmosphere from 300 to 900 K.

Thermal Transport Measurements: The thermal conductivity was calculated with the relationship $\kappa=\rho\lambda Cp$. The density ρ was determined using the dimensions and mass of the samples, respectively. The specific heat capacities and the diffusivities λ were measured using pellets cut and polished into square shapes of ~6×6×1.0 mm^3 and with the laser flash diffusivity method by LFA-457 (Netzsch, Germany), using the Pyroceram 9606 as a calibration standard.

Hall Measurements: The carrier concentration values were measured by the Van der Pauw method with an HMS-5500 Hall measurement system under a static magnetic field of 0.56 T.

Computational details

In this study, electrical properties were calculated based on the crystal cell (16 atoms: 4 Ag, 4 In, and 8 Se/Br) within a 7 × 7 × 3 mesh. The Perdew-Burke-Ernzerhof (PBE) with the generalized gradient approximation (GGA)[22] was used for exchange and correlation energy in structural optimization and band structure computations. In the Vienna Ab-initio Simulation Package (VASP)[23–26], the hybrid functional HSE06[27, 28] is further utilized to estimate the energy band. The cutoff energy for the wave function is 400 eV. To simplify the calculation, the phonon transport is calculated based on the original cell (8 atoms: 2 Ag, 2 In, and 4 Se). The anharmonic lattice dynamics of $AgInSe_2$ were calculated using temperature-dependent effective potential (TDEP)[29,30]. An energy cut-off of 400 eV was used throughout Ab initio molecular dynamics simulation. During molecular dynamics simulation, lattice parameters of a 2 × 2 × 4 supercell with 128 atoms were relaxed until the external pressure is smaller than 0.05 GPa. Then the results from molecular dynamics simulation were used to determine 2nd, 3rd, and 4th order force-constants (IFCs) by TDEP. The cut-offs for the 2nd, 3rd, and 4th order IFCs are 8.0 Å, 7.0 Å, and 4.5 Å, respectively.

Lattice thermal conductivity for 3ph scattering τ_{3ph}^{-1} was obtained by the Peierls-Boltzmann transport equation for phonons on a 26 × 26 × 26 mesh, as implemented in the software TDEP[31]. Since the full solution of the 4ph transport equation needs expensive calculations, the 4ph scattering process is accounted for in a non-self-consistent way. The 4ph scattering τ_{4ph}^{-1} rate was added to the total scattering rate τ^{-1} as:

$$\tau^{-1} = \tau_{3ph}^{-1} + \tau_{4ph}^{-1}. \quad (1)$$

The calculation of 4ph was carried out by interpolation method on an initial 6 × 6 ×6 mesh.

Results and discussion

$AgInSe_2$ is a semiconductor with a tetragonal structure and a wide bandgap of approximately 1.2 eV, which makes it suitable for various applications such as thermoelectricity, photovoltaic generation, and optical engineering[32,33]. The crystal structure of $AgInSe_2$ is diamond-like, with each Se atom bonded to two other elements Ag and In. The space group of $AgInSe_2$ is $I\bar{4}2d$ as shown in Fig. 1a. The difference in bond lengths between Ag-Se and In-Se provides a basis for the diversity of electron and phonon transport properties [8]. The carrier concentration of undoped $AgInSe_2$ at room temperat-

DOI: 10.54227/mlab.20230024

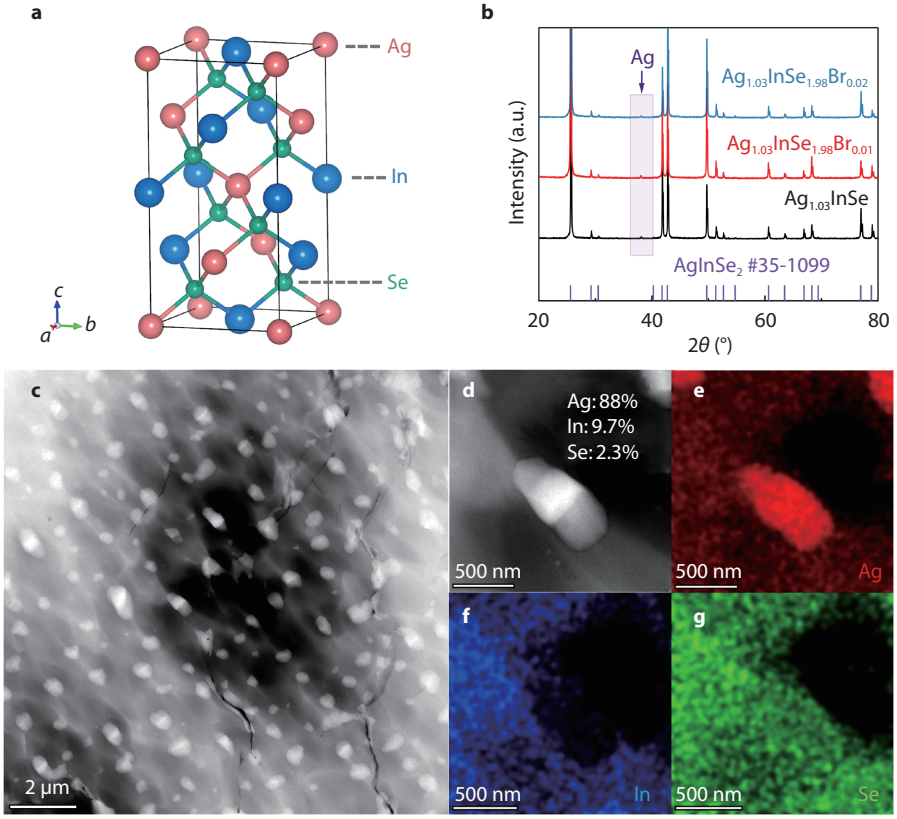


Fig. 1 **a** Crystal structure of $AgInSe_2$. **b** XRD patterns of $Ag_{1.03}InSe_{2-x}Br_x$ (x= 0, 0.01, and 0.02). Low magnification STEM HAADF image **c** magnified STEM HAADF image **d** and EDX (e-g) of $Ag_{1.03}InSe_2$.

ure is relatively low, ~1.3 × 10^{13} cm^{-3}, resulting in low electrical conductivity of 10^{-3} S cm^{-1}[34]. Due to the wide bandgap of $AgInSe_2$, free carriers are difficult to be excited in electronic transport. Furthermore, most chalcopyrites are naturally p-type due to cation vacancy, making it difficult to achieve high thermoelectric performance and n-type thermoelectric applications[9]. One approach to improve the conductivity of $AgInSe_2$ is through Ag doping[34]. As Figure S1 shows, compared with the experiment data of $AgInSe_2$ without excess Ag, the electrical conductivity of $Ag_{1.03}InSe_2$ is much higher, and the total thermal conductivity is lower. The resulting larger ZT values in a temperature range of 300-900 K mean that our strategy of 3% Ag over-doping, is effective. To improve the conductivity of $AgInSe_2$, 3% Ag over-doping is applied to each sample. This approach provides more electronic concentration than undoped $AgInSe_2$. The extranuclear 5s electrons in Ag provide extra electronic carriers for the whole system, resulting in a carrier concentration of 9.0 × 10^{15} cm^{-3} at room temperature for $Ag_{1.03}InSe_2$. This concentration is about three orders of magnitude higher than that of undoped $AgInSe_2$, which means that over-doping Ag is a very effective approach to improve the carrier concentration. In several n-type thermoelectric materials, the addition of Br dopants has been found to enhance the electronic concentration in chalcogenide compounds like SnS[35], SnSe[36], $SnSe_2$ [37], PbTe[38], and $AgBiSe_2$[39]. Thus, we introduced Br doping into $Ag_{1.03}InSe_2$ and synthesized a series of samples with varying Br content (x= 0, 0.01, and 0.02) by mixing the elements in stoichiometric proportions and then reacting them in the molten state. The resulting mixtures were consolidated into bulk using spark plasma sintering. The powder X-ray diffraction (XRD) patterns of the synthesized samples were recorded at room temperature and are presented in Fig. 1b. According to the PDF card (#No. 35-1099) of $AgInSe_2$, the secondary phase Ag is found in our sample. Scanning transmission electron microscopy high-angle annular dark field (STEM HAADF) images are shown in Fig. 1c, the STEM images reveal the presence of secondary phase precipitates homogeneously distributed throughout the matrix, with a size ranging from 500 nm to 2 μm. Energy-dispersive X-ray (EDX) spectroscopy analysis confirms that these precipitates consist mainly of Ag, with minor amounts of In and Se, thus verifying that the synthesized samples meet our desired specifications.

Our study also investigates the effect of Br doping on $AgInSe_2$ using ab initio calculations. The electronic band structures of $AgInSe_2$ and Br-doped $AgInSe_{1.75}Br_{0.25}$ are displayed in Fig. 2a and 2b, respectively. Both have a direct bandgap at the Γ high symmetry point, with the valence band maximum (VBM) and conduction band minimum (CBM) determined through calculation. The bandgap of $AgInSe_2$ is approximately 0.77 eV, which is lower than the experimental value due to ab initio calculations' tendency to underestimate the bandgap. While our model's precision may not be sufficient to determine the actual solid solubility of Br, our qualitative analysis shows that Br doping introduces the change of Fermi energy and enhances electronic concentration. We calculated the effective mass of holes and electrons by fitting a parabola to the CBM and VBM, respectively. The projected en-

DOI: 10.54227/mlab.20230024

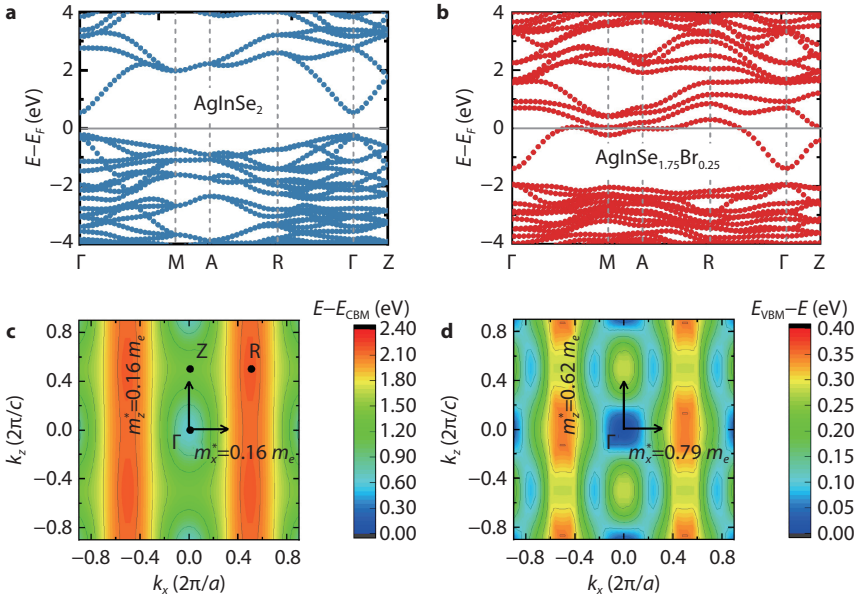


Fig. 2 Band structures of $AgInSe_2$ **a** and $AgInSe_{1.75}Br_{0.25}$ **b**, and Fermi energy E_F is set to be zero. Projection of band dispersion of the conduction **c** and valence **d** band energies for $AgInSe_2$ in the first Brillouin zone.

ergy band diagram of CBM (Fig. 2c) indicates an isotropic electronic effective mass of 0.16 m_e in both a and c directions, where m_e denotes electronic mass. The CBM in $AgInSe_2$ has only one valley, and the conduction band energy valley is isotropic, enabling the single parabolic band model to explain electronic transport properties [40]. The effective mass of the hole, as shown in Fig. 2d, is slightly anisotropic. The values of m_x^* and m_z^* are 0.79 and 0.62 m_e, respectively, which are relatively larger than those of the electron. Using the electronic effective mass for n-type $AgInSe_2$ at 300 K is 1.2×10^{18} cm^{-3} (details are provided in the Supplementary Information).

Fig. 3 displays the electronic transport properties of $Ag_{1.03}InSe_{2-x}Br_x$ (x= 0, 0.01, and 0.02). The comparison of other sample results, $Ag_{1.03}InSe_{2-x}Br_x$ (x= 0.005, 0.015), and the thermal and electrical transport properties of $AgInSe_2$ without excess Ag are shown in Fig. S1. $Ag_{1.03}InSe_{1.99}Br_{0.01}$ and $Ag_{1.03}InSe_{1.98}Br_{0.02}$ exhibit higher room temperature (RT) electrical conductivity, with values of 3.9 and 4.3 S cm^{-1}, respectively, compared to $Ag_{1.03}InSe_2$ (~1.6×10^{-3} S cm^{-1}). This increase in conductivity is due to the increase in electronic concentration and mobility. The electronic concentration of $Ag_{1.03}InSe_{2-x}Br_x$ (x= 0.01 and 0.02) at RT is 1.4×10^{17} and 4.3×10^{17} cm^{-3}, respectively. The relationship curves for the Seebeck coefficient and carrier concentration are shown in Fig. 3c, and the fitted electronic effective mass and relaxation time values are presented in Table 1. Comparing $Ag_{1.03}InSe_{1.99}Br_{0.01}$ and $Ag_{1.03}InSe_{1.98}Br_{0.02}$, the relaxation time remains virtually unchanged with increasing Br doping concentration, implying that the decrease in mobility is mainly caused by the increase in effective mass. The Seebeck coefficient values for $Ag_{1.03}InSe_{2-x}Br_x$ (x= 0.01 and 0.02) at RT are 3.0×10^2 and 3.6×10^2 μV K^{-1}, respectively. The absolute value of the Seebeck coefficient $|S|$ for $Ag_{1.03}InSe_2$ decreases with an increase in Br content (Fig. 3c). Additionally, $|S|$ for $Ag_{1.03}InSe_2$ sharply decreases in the temperature range of 300–400 K, which is a typical characteristic of two-band model dominant intrinsic semiconductors with a dramatic shift in Fermi energy, in general.[41] However, our DFT calculated band structure has shown that there is only one valley on CBM, which means the shift of Fermi energy has little contribution to electrical transport properties. Here, excess Br introduces many defects, which may enhance the energy-filtering effect. The electrons with lower energy are scattered by the defect barrier, only the electrons with high energy will cross the barrier, resulting in an increasing absolute value of the Seebeck coefficient. Compared to the results of the 1 % Br-doping sample, the electronic effective mass is enhanced due to the strong energy-filtering effect after 2 % doping, simultaneously. In addition, the *PF* of Br-doped $Ag_{1.03}InSe_2$ is significantly enhanced with a maximum value of 5.37 μW cm^{-1} K^{-2} at 900 K for $Ag_{1.03}InSe_{1.99}Br_{0.01}$. The measured data indicate that Br doping can increase electronic concentration and conductivity, which is consistent with our ab initio calculation results.

Fig. S1 displays the temperature-dependent total thermal conductivity $\kappa$of all samples. The total thermal conductivity comprises mainly two components, electronic and lattice thermal conductivity. The electronic thermal conductivity κ_e is determined by the Wiedemann-Franz relationship, $\kappa_e = LT\sigma$, where L denotes the Lorenz number. The lattice thermal conductivity (Fig. 4a) obtained for all samples exhibits similar RT values of approximately 0.85 W m^{-1} K^{-1}, which suggests that Br doping has a weak effect on thermal transport. Compared to other conventional thermoelectric materials, such as Bi_2Te_3 (0.7 W m^{-1} K^{-1}), PbTe (0.8 W m^{-1} K^{-1}), and SnSe (1.3 W m^{-1} K^{-1}), $AgInSe_2$ demonstrates relatively low lattice thermal conductivity.

To further investigate the origin of the low lattice thermal conductivity of $AgInSe_2$, the phonon dispersion at 300 K was calculated, as illustrated in Fig. 4b. Low-frequency optical phonons were observed around 4 meV, which partially overlap with the acoustic phonons. Many avoided-crossing points were identified between the low-frequency optical phonons

DOI: 10.54227/mlab.20230024

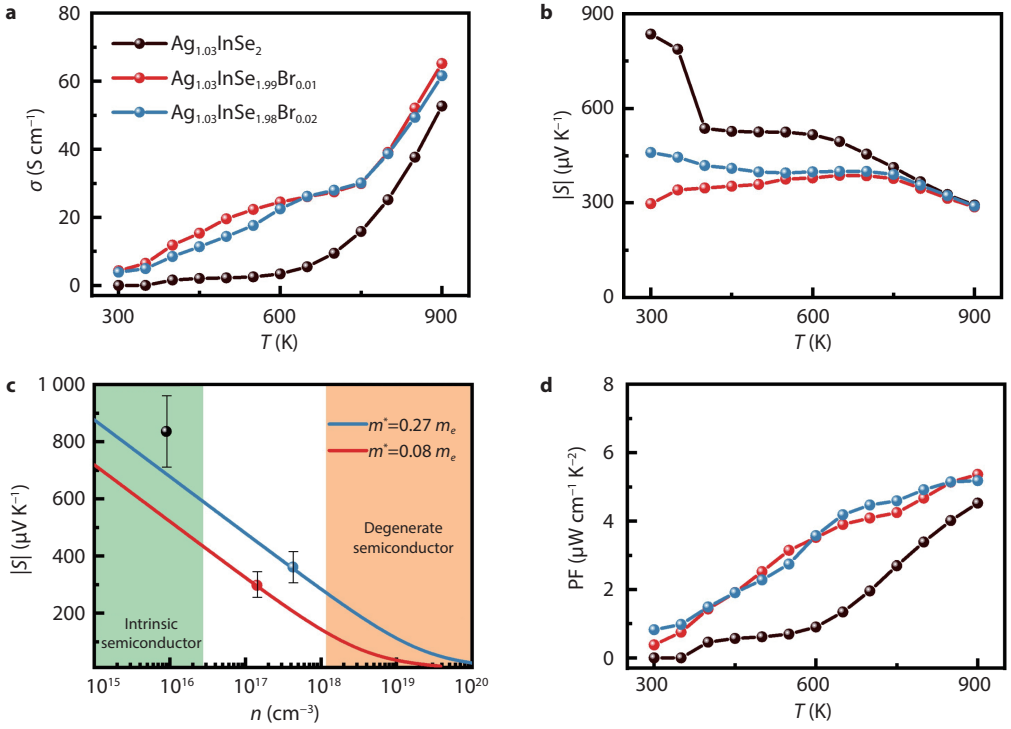


Fig. 3 **a** Electrical conductivity σ, **b** Seebeck coefficient S and **d** PF of all samples from 300 to 900 K. **c** Electronic concentration n dependent Seebeck coefficient S for all samples at RT. The solid lines are calculated according to the single parabolic band model. The green and yellow regions represent the range of intrinsic semiconductors and degenerate semiconductors, respectively.

Table 1. Electrical conductivity σ, carrier concentration n, mobility μ, electronic effective mass m^* obtained by single parabolic band model, electronic relaxation time τ of all samples at RT.

Samples	σ	n	M	m^*	τ
	S cm^{-1}	cm^{-3}	cm^2 V^{-1} s^{-1}	m_e	fs
$Ag_{1.03}InSe_2$	1.6×10^{-3}	9.0×10^{15}	1.1	0.8	5.1×10^{-1}
$Ag_{1.03}InSe_{1.99}Br_{0.01}$	3.9	1.4×10^{17}	1.9×10^{2}	0.08	8.6
$Ag_{1.03}InSe_{1.98}Br_{0.02}$	4.3	4.3×10^{17}	5.7×10^{1}	0.27	8.8

and acoustic phonons along the path from the zone center Γ point to the boundary of the Brillouin zone, leading to a strong coupling effect between phonons. Furthermore, the acoustic branch and low-frequency optical branch display many flat dispersions, providing significant 4ph scattering phase space. The localized low-frequency acoustic phonon also implies low group velocities. These nondispersive low-frequency phonon dispersions are highly significant and suggest that strong phonon coupling excites not only 3ph but also 4ph interaction in thermal transport. Fig. S2 vividly demonstrates the 3ph and 4ph scattering processes. In 3ph scattering processes, two phonons (k_1 and k_2) combine to create a new phonon (k_3). According to the law of energy conservation ($\hbar\omega_{k_1} + \hbar\omega_{k_2} = \hbar\omega_{k_3}$ where $\hbar$ is reduced Planck constant and ω is phonon frequency), the newly generated phonon energy must be higher than $\hbar\omega_{k_1}$ or $\hbar\omega_{k_2}$. This results in limited 3ph scattering when there is no higher energy phonon branch (dashed in Figure S2). However, in the 4ph scattering recombination processes, two phonons (k_1 and k_2) combine into two new phonons(k_3 and k_4), are permitted. If two phonon branches are parallel, both the laws of energy conservation ($\hbar\omega_{k_1} + \hbar\omega_{k_2} = \hbar\omega_{k_3} + \hbar\omega_{k_4}$) and momentum conservation ($k_1 + k_2 = k_3 + k_4 + G$ where G is a reciprocal lattice vector) are met. As a result, the cumulative 4ph scattering phase space is enormous, and 4ph must be considered in phonon transport. The projected phonon DOS (Fig. 4c) shows that low-frequency phonons with an energy of ~4 meV mainly come from Ag, which can be the reason for the strong phonon-phonon coupling.[12].

To further confirm the significant role of 4ph in phonon transport in $AgInSe_2$, we directly performed lattice dynamics calculations for anharmonic phonons, as detailed in the Supplementary Information. Fig. 4d shows the lineshape peaks ω_0 of the transverse acoustic (TA) and longitudinal acoustic (LA) phonon spectrum functions at the P point, which are 3.2 meV and 4.1 meV, respectively. The imaginary part of phonon self-energy functions Γ_ω is closely related to the phonon scattering rate τ^{-1}, where $\tau^{-1} = 2\Gamma_\omega(\omega_0)$.[12] At the characteristic frequency of the TA phonon (3.2 meV), the imaginary part of the 4ph is comparable to that of the 3ph. Additionally, at the characteristic frequency of the LA phonon (4.1 meV), the 4ph imaginary part is only slightly smaller than the 3ph imaginary part. This behavior is common for both TA and LA modes, as seen in Fig. S3 where the intensity of 4ph phonon

DOI: 10.54227/mlab.20230024

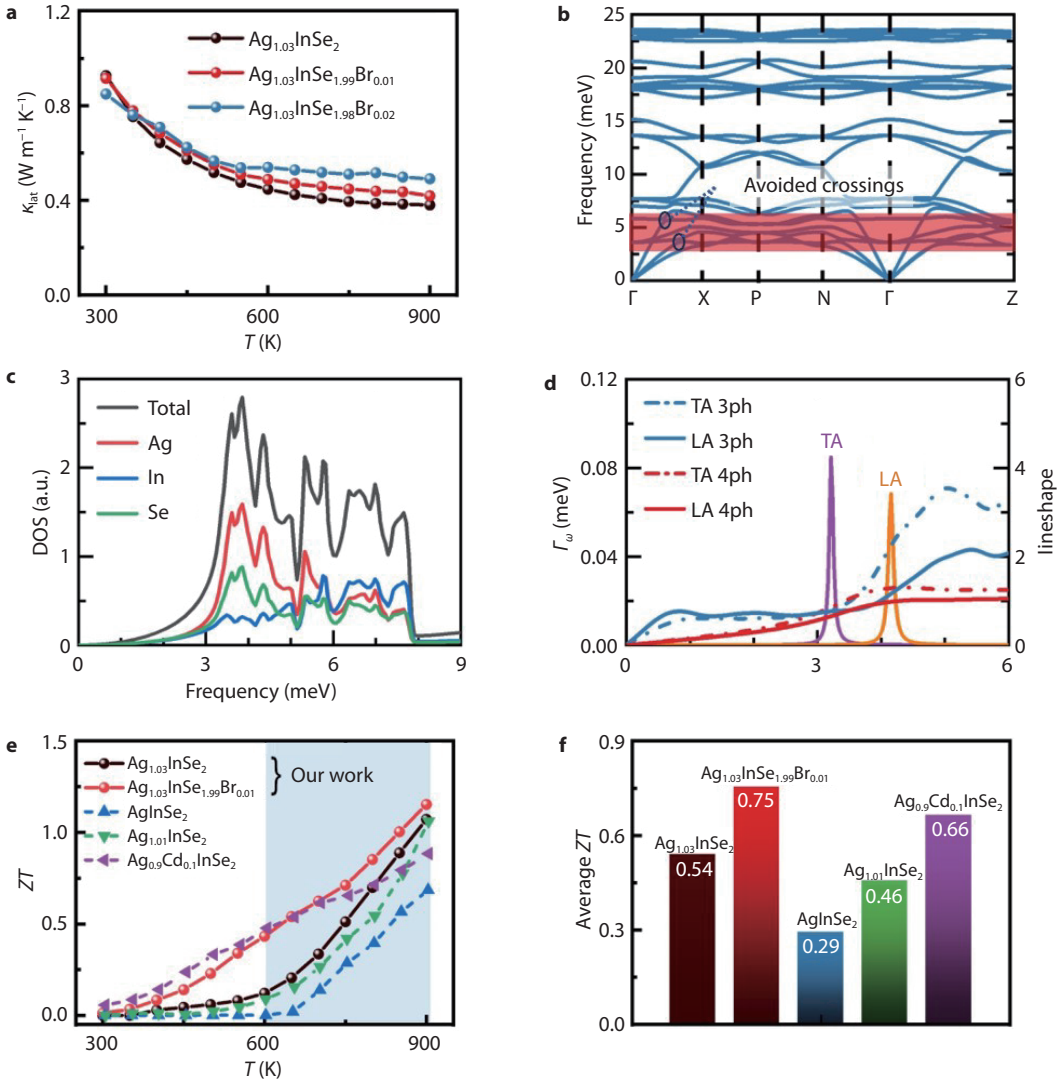


Fig. 4 **a** Lattice thermal conductivity κ_{lat} of all samples from 300 to 900 K. **b** Calculated phonon dispersion and **c** phonon DOS of $AgInSe_2$. **d** 4 curves that increase as phonon frequency rises represent the imaginary part Γ_ω of the 3ph and 4ph self-energy functions at P point, and the purple and orange peak lines represent the lineshape of TA and LA at P point, respectively. **e** *ZT* and **f** average *ZT* (from 600 to 900 K) of all samples and other reported $AgInSe_2$ materials [34, 44].

scattering is not lower than that of 3ph scattering at the Z point. Thus, 4ph interactions should not be ignored. The lattice thermal conductivity of 3ph interaction was calculated to be 2.1 W m^{-1} K^{-1} in *a* direction and 2.3 W m^{-1} K^{-1} in *c* direction, while the lattice thermal conductivity of 3ph and 4ph interactions was found to be 0.8 W m^{-1} K^{-1} in *a* direction and 0.9 W m^{-1} K^{-1} in *c* direction, respectively. The theoretical lattice thermal conductivity, taking into account the 4ph interaction, is in perfect agreement with the experimental value (Fig. S4)[9,42,43]. Therefore, the underlying cause of the intrinsic low thermal conductivity in $AgInSe_2$ can be attributed to the four-phonon interaction. Fig. 4e shows the temperature-dependent *ZT* of various $AgInSe_2$ samples, including $AgInSe_2$, $Ag_{1.01}InSe_2$, $Ag_{1.03}InSe_2$, $Ag_{0.9}Cd_{0.1}InSe_2$, and $Ag_{1.03}InSe_{1.99}Br_{0.01}$. The addition of 1% Br doping significantly enhances the electronic transport performance without substantially increasing the lattice thermal conductivity. Compared to undoped $AgInSe_2$, the *ZT* value of $Ag_{1.03}InSe_{1.99}Br_{0.01}$ increases from 0.7 to 1.2 at 900 K, achieving an average *ZT* of 0.75 over the temperature range of 600 to 900 K, which is comparable to many reported p-type chalcopyrite compounds.

Conclusions

In summary, we have successfully prepared Br-doped n-type $AgInSe_2$ with outstanding thermoelectric performance. Preparation of the n-type chalcopyrite materials has been a notable challenge primarily due to inherent cation vacancies. However, through the suppression of Ag vacancies using excessive Ag and the optimization of electronic transport via Br doping, n-type $AgInSe_2$ has been successfully achieved. This offers a viable method to hinder persistent cation vacancies in intrinsic p-type semiconductors while obtaining n-type semiconductors. It brings forth new insights into the design of thermoelectric devices aiming to acquire n-type counterparts for intrinsic p-type thermoelectric materials. In terms of

DOI: 10.54227/mlab.20230024

thermal transport, ultralow lattice thermal conductivity is a crucial factor for ensuring excellent thermoelectric properties. The flat low-frequency phonon dispersion and avoided crossovers between acoustic phonons and low-frequency optical phonons in $AgInSe_2$ are the characteristics of strong phonon coupling. In general, 3ph scattering is dominant in most of the materials, whereas the high-order phonon scattering phase space is significantly enhanced in strong phonon coupling materials, which results in ultralow lattice thermal conductivity. This provides a new perspective for the high-throughput screening of potential high-performance thermoelectric materials with ultralow lattice thermal conductivity.

■ ACKNOWLEDGMENTS

This work was supported by the National Natural Science Foundation of China (Grant No. 11934007, 11874194, and 12174176), the Science and Technology Innovation Committee Foundation of Shenzhen (Grant No. JCYJ20200109141205978, JCYJ20190809145205497), and the Outstanding Talents Training Fund in Shenzhen (2021108).

■ CONFLICT OF INTEREST

The authors declare no conflict of interest.

■ AUTHOR CONTRIBUTIONS

S. H. and J. Q. H. designed this work. Y. W. and L. X. performed the calculations. B. H. J. synthesized the samples and carried out the transport property measurements. B. H. J., Y. Y, and P. J. L. carried out the experimental study and performed the TEM observations. S. H., Y. W., and J. Q. H. wrote and all authors edited this manuscript.

■ REFERENCES

1. J. P. Heremans, B. Wiendlocha and A. M. Chamoire, *Energy Environ. Sci.*, 2012, 5, 5510
2. C. Y. Fong and C. Kittel, *Am. J. Phys.*, 1967, 35, 1091
3. J. He and T. M. Tritt, *Science*, 2017, 357, eaak9997
4. S. I. Kim, K. H. Lee, H. A. Mun, H. S. Kim, S. W. Hwang, J. W. Roh, D. J. Yang, W. H. Shin, X. S. Li, Y. H. Lee, G. J. Snyder and S. W. Kim, *Science*, 2015, 348, 109
5. S. Bathula, M. Jayasimhadri, N. Singh, A. K. Srivastava, J. Pulikkotil, A. Dhar and R. C. Budhani, *Appl. Phys. Lett.*, 2012, 101, 213902
6. N. Yang, C. Chen, L. Pan, Y. Zhao and Y. Wang, *J. Alloys Compd.*, 2020, 847, 156410
7. J. Zhang, L. Huang, C. Zhu, C. Zhou, B. Jabar, J. Li, X. Zhu, L. Wang, C. Song, H. Xin, D. Li and X. Qin, *Adv. Mater.*, 2019, 31, 1905210
8. Y. Cao, X. Su, F. Meng, T. P. Bailey, J. Zhao, H. Xie, J. He, C. Uher and X. Tang, *Adv. Funct. Mater.*, 2020, 30, 2005861
9. J. J. Plata, V. Posligua, A. M. Márquez, J. F. Sanz and R. Grau-Crespo, *Chem. Mater.*, 2022, 34, 2833
10. X. Su, N. Zhao, S. Hao, C. C. Stoumpos, M. Liu, H. Chen, H. Xie, Q. Zhang, C. Wolverton, X. Tang and M. G. Kanatzidis, *Adv. Funct. Mater.*, 2019, 29, 1806534
11. Y. Zhu, B. Wei, J. Liu, N. Z. Koocher, Y. Li, L. Hu, W. He, G. Deng, W. Xu, X. Wang, J. M. Rondinelli, L.-D. Zhao, G. J. Snyder and J. Hong, *Mat. Today Phys.*, 2021, 19, 100428
12. L. Xie, J. H. Feng, R. Li and J. Q. He, *Phys. Rev. Lett.*, 2020, 125, 245901
13. T. Feng, L. Lindsay and X. Ruan, *Phys. Rev. B*, 2017, 96, 161201(R)
14. X. Xu, J. Cui, Y. Yu, B. Zhu, Y. Huang, L. Xie, D. Wu and J. He, *Energy Environ. Sci.*, 2020, 13, 5135
15. X. Xu, Y. Huang, L. Xie, D. Wu, Z. Ge and J. He, *Chem. Mater.*, 2020, 32, 1693
16. B. Zhu, X. Liu, Q. Wang, Y. Qiu, Z. Shu, Z. Guo, Y. Tong, J. Cui, M. Gu and J. He, *Energy Environ. Sci.*, 2020, 13, 2106
17. B. Zhu, W. Wang, J. Cui and J. He, *Small*, 2021, 17, 2101328
18. X. Yang, T. Feng, J. Li and X. Ruan, *Phys. Rev. B*, 2019, 100, 245203
19. T. Feng and X. Ruan, *Phys. Rev. B*, 2018, 97, 045202
20. Z. Han, X. Yang, W. Li, T. Feng and X. Ruan, *Phys. Commun.*, 2022, 270, 108179
21. T. Feng and X. Ruan, *Phys. Rev. B*, 2016, 93, 045202
22. J. P. Perdew, K. Burke, M. Ernzerhof, *Phys. Rev. Lett.*, 1996, 77, 3865
23. G. Kresse, J. Hafner, *Phys. Rev. B.*, 1993, 47, 558(R)
24. G. Kresse, J. Hafner, *J. Phys.: Condens. Matter.*, 1994, 6, 8245
25. G. Kresse, J. Furthmüller, *Comput. Mater. Sci.*, 1996, 6, 15
26. G. Kresse, J. Furthmüller, *Phys. Rev. B.*, 1996, 54, 11169
27. J. Heyd, G. E. Scuseria, *J. Chem. Phys.*, 2004, 121, 1187
28. J. Heyd, G. E. Scuseria, M. Ernzerhof, *J. Chem. Phys.*, 2003, 118, 8207
29. O. Hellman, I. A. Abrikosov, S. I. Simak, *Phys. Rev. B.*, 2011, 84, 180301
30. O. Hellman, P. Steneteg, I. A. Abrikosov, S. I. Simak, *Phys. Rev. B*, 2013, 87, 104111
31. O. Hellman, D. A. Broido, *Phys. Rev. B.*, 2014, 90, 134309
32. J. L. Shay, B. Tell, H. M. Kasper and L. M. Schiavone, *Phys. Rev. B*, 1973, 7, 4485
33. K. Koitabashi, S. Ozaki and S. Adachi, *J. Appl. Phys.*, 2010, 107, 053516
34. P. Qiu, Y. Qin, Q. Zhang, R. Li, J. Yang, Q. Song, Y. Tang, S. Bai, X. Shi and L. Chen, *Adv. Sci.*, 2018, 5, 1700727
35. X. Hu, W. He, D. Wang, B. Yuan, Z. Huang and L.-D. Zhao, *Scr. Mater.*, 2019, 170, 99
36. L. Su, T. Hong, D. Wang, S. Wang, B. Qin, M. Zhang, X. Gao, C. Chang and L.-D. Zhao, *Mater. Today Phys.*, 2021, 20, 100452
37. C. Zhou, Y. Yu, X. Zhang, Y. Cheng, J. Xu, Y. K. Lee, B. Yoo, O. Cojocaru-Mirédin, G. Liu, S.-P. Cho, M. Wuttig, T. Hyeon and I. Chung, *Adv. Funct. Mater.*, 2020, 30, 1908405
38. Y. Dong, M. A. McGuire, A.-S. Malik and F. J. DiSalvo, *J. Solid State Chem.*, 2009, 182, 2602
39. S. N. Guin, V. Srihari and K. Biswas, *J. Mater. Chem. A*, 2015, 3, 648
40. H. Lee, *Thermoelectrics: Design and Materials*, John Wiley & Sons, America, 2016.
41. T. C. Chasapis, D. Koumoulis, B. Leung, N. P. Calta, S.-H. Lo, V. P. Dravid, L.-S. Bouchard and M. G. Kanatzidis, *APL Mater.*, 2015, 3, 083601
42. Y. Zhu, Y. Liu, M. Wood, N. Z. Koocher, Y. Liu, L. Liu, T. Hu, J. M. Rondinelli, J. Hong, G. J. Snyder and W. Xu, *Chem. Mater.*, 2019, 31, 8182
43. L. Wang, P. Ying, Y. Deng, H. Zhou, Z. Du and J. Cui, *RSC Adv.*, 2014, 4, 33897
44. Y. Zhong, Y. Luo, X. Li and J. Cui, *ACS Appl. Energy Mater.*, 2020, 3, 12468

©2024 The Authors. *Materials Lab* is published by Lab Academic Press. This is an open access article under the terms of the Creative Commons Attribution License, which permits use, distribution and reproduction in any medium, provided the original work is properly cited.